

Article

g-CN/ NiAl-LDH 2D/2D Hybrid Heterojunction for High-Performance Photocatalytic Reduction of CO into Renewable Fuels

Surendar Tonda, Santosh Kumar, Monika Bhardwaj, Poonam Yadav, and Satishchandra Ogale

ACS Appl. Mater. Interfaces, **Just Accepted Manuscript** • DOI: 10.1021/acsami.7b18835 • Publication Date (Web): 29 Dec 2017Downloaded from <http://pubs.acs.org> on January 2, 2018**Just Accepted**

“Just Accepted” manuscripts have been peer-reviewed and accepted for publication. They are posted online prior to technical editing, formatting for publication and author proofing. The American Chemical Society provides “Just Accepted” as a free service to the research community to expedite the dissemination of scientific material as soon as possible after acceptance. “Just Accepted” manuscripts appear in full in PDF format accompanied by an HTML abstract. “Just Accepted” manuscripts have been fully peer reviewed, but should not be considered the official version of record. They are accessible to all readers and citable by the Digital Object Identifier (DOI®). “Just Accepted” is an optional service offered to authors. Therefore, the “Just Accepted” Web site may not include all articles that will be published in the journal. After a manuscript is technically edited and formatted, it will be removed from the “Just Accepted” Web site and published as an ASAP article. Note that technical editing may introduce minor changes to the manuscript text and/or graphics which could affect content, and all legal disclaimers and ethical guidelines that apply to the journal pertain. ACS cannot be held responsible for errors or consequences arising from the use of information contained in these “Just Accepted” manuscripts.



1
2
3 **g-C₃N₄/ NiAl-LDH 2D/2D Hybrid Heterojunction for High-Performance Photocatalytic**
4
5
6 **Reduction of CO₂ into Renewable Fuels**
7

8
9 Surendar Tonda,^a Santosh Kumar,^b Monika Bhardwaj,^c Poonam Yadav,^d and Satishchandra
10
11 Ogale^{c,*}
12
13
14
15

16 ^a Department of Chemistry and Centre for Energy Science, Indian Institute of Science Education
17 and Research, Dr. Homi Bhabha Road, Pashan, Pune 411008, India
18
19

20
21 ^b European Bioenergy Research Institute, Aston University, Birmingham B4 7ET, UK
22
23

24 ^d Physical and Materials Chemistry Division, National Chemical Laboratory (CSIR-NCL),
25 Pashan, Pune 411008, India
26
27
28

29
30 ^c Department of Physics and Centre for Energy Science, Indian Institute of Science Education
31 and Research, Dr. Homi Bhabha Road, Pashan, Pune 411008, India
32
33
34
35
36
37

38 ***Corresponding Author:**
39

40
41 Satishchandra Ogale, E-mail: satishogale@iiserpune.ac.in; satishogale@gmail.com, Tel.: +91 20
42
43 2590 8292.
44
45
46
47
48
49
50
51
52
53
54
55
56
57

ABSTRACT

2D/2D interface heterostructures of g-C₃N₄ and NiAl-LDH are synthesized utilizing strong electrostatic interactions between positively charged 2D NiAl-LDH sheets and negatively charged 2D g-C₃N₄ nanosheets. This new 2D/2D interface heterojunction showed remarkable performance for photocatalytic CO₂ reduction to produce renewable fuels such as CO and H₂ under visible-light irradiation, far superior to that of either single phase g-C₃N₄ or NiAl-LDH nanosheets. The enhancement of photocatalytic activity could be attributed mainly to the excellent interfacial contact at the heterojunction of g-C₃N₄/NiAl-LDH, which subsequently results in suppressed recombination, and improved transfer and separation of photogenerated charge carriers. In addition, the optimal g-C₃N₄/NiAl-LDH nanocomposite possessed high photostability after successive experimental runs with no obvious change in the production of CO from CO₂ reduction. Our findings regarding the design, fabrication and photophysical properties of 2D/2D heterostructure systems may find use in other photocatalytic applications including H₂ production and water purification.

KEYWORDS: layered double hydroxide, g-C₃N₄, CO₂ reduction, nanocomposite, photocatalysis

1. INTRODUCTION

One of the foremost challenges faced by today's human society is to conserve the environment for future generations, especially in light of concerns about global climate change related to rapid increase of atmospheric carbon dioxide (CO₂) levels. In addition to anthropogenic CO₂ emissions, human beings are also facing the ever-increasing challenge of the inevitable depletion of fossil fuel resources.¹⁻³ In this scenario, the development of novel technologies for the sustainable production of energy in an environmentally and economically feasible manner is urgently required. The conversion of CO₂ into renewable fuels by using clean and abundant solar energy, mimicking natural photosynthesis, has been regarded as one of the most compelling strategies that would not only reduce the atmospheric CO₂ levels but promises to fulfill the global energy demands.^{4,5} Since the discovery of photoconversion of CO₂ to valuable fuels such as CH₃OH, CH₄, HCHO and HCOOH over semiconductor aqueous suspension by Inoue and co-workers in 1979,⁶ great efforts have been made to construct more efficient and environmentally friendly catalysts to attain CO₂ photo-conversion more economically. However, the reduction of CO₂ is quite challenging owing to its thermodynamically inert and stable properties. Therefore, search for highly efficient and stable photocatalysts for CO₂ conversion, especially under solar light irradiation is a central challenge in this area of research.

In recent years, graphitic carbon nitride (g-C₃N₄), a metal-free conjugated polymer semiconductor has emerged as a promising alternative to the various traditional metal-containing photocatalysts, such as oxides,^{7,8} sulfides,^{9,10} and oxynitrides,¹¹ due to its fascinated properties such as high physicochemical stability, narrow band gap (2.7 eV), tunable electronic structure, low cost, non-toxicity, and most importantly, appropriate band edge potentials for water splitting and CO₂ photoreduction.¹²⁻¹⁵ However, practical applications of pure g-C₃N₄ are still hindered by

1
2
3 several obstacles and shortcomings including rapid recombination of charge carriers, low
4 specific surface area, and its low utilization efficiency of light quanta. With the aim to eradicate
5 these obstacles, many attempts have been made to further improve the performance of pure g-
6 C_3N_4 including electronic structure modulation,¹⁶ combining it with other conducting
7 materials,^{14,17} constructing its heterojunction with other semiconductors,¹⁸⁻²¹ and loading co-
8 catalysts.^{22,23} Among all the strategies, the construction of heterojunctions by combining two
9 different semiconductors, particularly two-dimensional (2D) layered architectures with suitable
10 conduction and valence band potentials is one of the most effective approaches to enhance the
11 separation efficiency of photogenerated charge carriers during the photocatalytic process.²⁴⁻²⁷ For
12 instance, Xiang et al.²⁸ developed 2D/2D g- C_3N_4 /graphene heterostructures, and their
13 photocatalytic activities were investigated for H_2 production under hole sacrificial agent. Very
14 recently, Liu and co-workers²⁹ synthesized a 2D/2D $CdIn_2S_4$ /mpg- C_3N_4 heterostructure for
15 photocatalytic CO_2 reduction to generate methanol. Despite great efforts, the photocatalytic
16 efficiency, particularly for CO_2 reduction without using a sacrificial agent, is still an open
17 challenge due not only to slow redox chemistry but also issues related to the efficacy of CO_2
18 adsorption and electron transfer to CO_2 .

19
20
21
22
23
24
25
26
27
28
29
30
31
32
33
34
35
36
37
38
39
40 In this work, we have successfully constructed a heterojunction between the negatively
41 charged 2D g- C_3N_4 nanosheets and positively charged NiAl-layered double hydroxide (NiAl-
42 LDH). Owing to the 2D layered configuration, band structure matching with favourable redox
43 chemistry, basicity of surface hydroxyl groups, visible-light-absorption capability, NiAl-LDH is
44 a great choice to be coupled with g- C_3N_4 to create 2D/2D intimate interface at the heterojunction
45 with excellent charge carrier mobility with expected high CO_2 availability on the surface.³⁰⁻³⁶
46
47
48
49
50
51
52
53
54 More attractively, as shown in this work, this heterostructure exhibits a high performance for
55
56
57
58
59
60

1
2
3 photocatalytic CO₂ reduction under visible-light irradiation. Our results clearly establish that the
4 coupling of 2D g-C₃N₄ nanosheets with basic 2D NiAl-LDH nanosheets plays a vital role in not
5 only reducing charge recombination and improving the charge transfer but also improved CO₂
6 adsorption and electron transfer to CO₂. Moreover, NiAl-LDH coupled g-C₃N₄ nanosheets is a
7 low cost material, which could be a potential candidate in practical applications such as
8 photocatalytic CO₂ reduction without using a sacrificial agent. To the best of our knowledge, this
9 is the first report on the use of the 2D layered junction between g-C₃N₄ nanosheets and NiAl-
10 LDH for the visible-light-driven photocatalytic CO₂ reduction to generate solar fuels.
11
12
13
14
15
16
17
18
19
20
21
22
23

24 **2. EXPERIMENTAL SECTION**

25
26
27
28 **2.1 Materials.** Nickel nitrate hexahydrate (Merck, AR grade), aluminum nitrate nonahydrate
29 (Merck, AR grade), melamine (Sigma-Aldrich, 99.0%), ammonium fluoride (SDFCL, AR grade)
30 and urea (SDFCL, AR grade) were used as received. All other chemicals used in this work were
31 of analytical grade and used as-received without further purification. All aqueous solutions were
32 prepared with Milli-Q water.
33
34
35
36
37
38

39
40 **2.2 Method.** The pure g-C₃N₄ nanosheets were synthesized according to a procedure
41 described in our previous paper.³⁷ Initially, bulk g-C₃N₄ was synthesized by a simple thermal
42 condensation method using melamine as a precursor. Approximately 10 g of melamine was
43 placed in an alumina combustion boat and thermally treated at 550 °C for 2 h in a tube furnace
44 with a heating rate of 5 °C min⁻¹ under N₂ atmosphere. The obtained yellow agglomerates was
45 ground into fine powder and collected for further use. The g-C₃N₄ nanosheets were synthesized
46 by ultrasonic exfoliation of the obtained bulk g-C₃N₄ in water. About 100 mg of bulk g-C₃N₄ was
47 dispersed in 250 mL of water, followed by ultrasonic treatment for 15 h. The obtained
48
49
50
51
52
53
54
55
56
57
58
59
60

1
2
3 suspension was centrifuged at low rpm to separate the residual unexfoliated g-C₃N₄. Then the
4
5 supernatant suspension was heated to remove water and the so-obtained pale yellow powder of
6
7 g-C₃N₄ nanosheets was denoted as CN.
8
9

10 The flower-like pure NiAl-LDH was synthesized according to the reported synthesis
11 procedure with some modifications mentioned below.³⁸ The g-C₃N₄/NiAl-LDH composites were
12 synthesized by a one-step *in situ* hydrothermal method. In a typical process, a calculated amount
13 of as-synthesized g-C₃N₄ nanosheets was dispersed in 80 mL of water and subjected to
14 ultrasonication for 30 min. Then, Ni(NO₃)₂·6H₂O (0.006 M) and Al(NO₃)₃·9H₂O (0.002 M) were
15 added into the above g-C₃N₄ suspension and ultrasonicated for another 10 min. Subsequently,
16 NH₄F (0.016 M) and urea (0.04 M) were dissolved into the mixed solution and stirred for 30
17 min. The obtained suspension was thermally treated in a sealed Teflon-lined autoclave (100 mL)
18 at 120 °C for 24 h. The resulting precipitate was washed with water several times until the pH
19 reached 7 and dried in an oven at 60 °C overnight. A series of g-C₃N₄/NiAl-LDH 2D/2D
20 composites with 5, 10, 15 and 20 wt.% NiAl-LDH to g-C₃N₄ were synthesized and denoted as
21 CNLDH-5, CNLDH-10, CNLDH-15, and CNLDH-20, respectively. Pure NiAl-LDH was also
22 synthesized by a similar procedure in the absence of g-C₃N₄, but without ultrasonication
23 throughout the reaction.
24
25
26
27
28
29
30
31
32
33
34
35
36
37
38
39
40
41

42 **2.3 Materials Characterization.** X-ray diffraction (XRD) measurements were conducted on
43 a Bruker D8-Advance X-ray diffractometer operating with Cu K_α radiation ($\lambda = 1.5418 \text{ \AA}$) over
44 the 2 θ range of 10–80°. The ultraviolet–visible diffuse reflectance spectra (UV–vis DRS) of
45 samples were recorded over the range of 250–800 nm using a UV-3600, Shimadzu (UV–vis NIR
46 spectrophotometer) equipped with an integrating sphere, and BaSO₄ was used as a reference. The
47 Fourier transform infrared (FT-IR) spectra of the samples were recorded using a PerkinElmer
48
49
50
51
52
53
54
55
56
57
58
59
60

1
2
3 Spectrum 100 FT-IR spectrophotometer with a resolution of 4 cm^{-1} . Photoluminescence (PL)
4 spectra of the samples were conducted at room temperature on a steady state spectrofluorometer
5 (SHIMADZU RF-6000) with an excitation wavelength of 365 nm. Transmission electron
6 microscopy (TEM) and high-resolution TEM (HRTEM) measurements were performed on a FEI
7 Tecnai G² transmission electron microscope, operated at 200 kV. X-ray photoelectron
8 spectroscopy (XPS) measurements were carried out on a PHI 5000 versaprobe instrument
9 (ULVAC-PHI, Chigasaki, Japan) with monochromatic Al K α X-ray radiation. The thermo-
10 gravimetric analysis (TGA) was performed on a PerkinElmer Pyris Diamond TGA/DTA
11 instrument. Nitrogen adsorption–desorption isotherms were carried out on a BELSORP-max,
12 (Japan) equipment.

26 **2.4 Photoelectrochemical Measurements.** Photoelectrochemical measurements were carried
27 out on an IVIUM Technologies electrochemical workstation with a standard three-electrode
28 photoelectrochemical cell. 0.1 M Na₂SO₄ was used as the electrolyte solution. Indium Tin Oxide
29 (ITO) deposited with photocatalyst served as a working electrode, while the counter and the
30 reference electrodes were platinum wire and Ag/AgCl (in saturated KCl), respectively.
31 Photocurrent measurements of the synthesized photocatalysts were examined for several on-off
32 cycles of light irradiation by a 300 W Xenon arc lamp. The typical working electrode preparation
33 was as follows: 20 mg of a powder sample was dispersed in 0.5 mL of ethanol and 20 μL of
34 Nafion solution (5 wt%), and then ground well to make uniform slurry. The obtained slurry was
35 then deposited as a thin film onto the ITO glass substrate, and the coated area was fixed at 1.0
36 cm^2 . Finally, the coated ITO glass was dried at 80 °C to obtain a homogeneous film.

51 **2.5 Evaluation of Photocatalytic Activity.** Photocatalytic activity of the synthesized samples
52 for CO₂ reduction was evaluated in gaseous phase in a 250 mL stainless steel photoreactor with a
53

1
2
3 quartz window. A 300 W Xenon arc lamp was used as the light source with a UV cut-off filter (λ
4 ≥ 420 nm). In a typical process, 50 mg of the powder sample was placed into a photoreactor.
5
6 Prior to irradiation, the reaction setup was vacuum-treated and purged with high purity CO₂ gas
7
8 (5 ml/min) for 1 h, to remove air from the system. The high purity CO₂ gas was led to pass
9
10 through a water bubbler to generate a mixture of CO₂ and water vapor. During the irradiation, 1
11
12 mL gaseous products from the reaction chamber were sampled at given time intervals (1 h) for
13
14 subsequent quantitative analysis of products by using gas chromatograph (Shimadzu Tracera
15
16 GC-2010 Plus) with Barrier Ionization Detector and He as a carrier gas. For reusability/stability
17
18 test, the selected photocatalyst was collected after each run and refreshed by washing with water
19
20 and heat treatment at 100 °C, and its photocatalytic activity was reevaluated under the
21
22 aforementioned conditions.
23
24
25
26
27

28 The selectivity towards reactively-formed CO was simply deduced according to the following
29
30 equation.³⁶
31

$$32 \text{ CO Selectivity (\%)} = \frac{2N_{\text{CO}}}{2N_{\text{CO}} + 2N_{\text{H}_2}} \times 100$$

33
34 In which N_{CO} and N_{H₂} stand for the yields of reactively-formed CO and H₂, respectively.
35
36
37

38 Apparent quantum yield (AQY) of the photocatalyst was calculated using the following
39
40 equation according to previously reported works.³⁹⁻⁴¹
41
42

$$43 \text{ AQY (\%)} = \frac{\text{the no of reacted electrons}}{\text{the no of incident photons}} \times 100$$
$$44 = \frac{\text{the no of evolved CO molecules} \times 2}{\text{the no of incident photons}} \times 100$$

45
46
47 (AQY calculations are explained in the supporting information)
48
49
50
51
52
53
54

3. RESULTS AND DISCUSSION

3.1. Formation Process and Characterization of g-C₃N₄/NiAl-LDH Heterojunctions. In the present study, the g-C₃N₄/NiAl-LDH nanocomposites are synthesized by a facile one-step *in situ* hydrothermal method and the formation process is schematically illustrated in **Scheme 1**. Initially, g-C₃N₄ nanosheets were obtained by ultrasonic exfoliation of the bulk g-C₃N₄ in water. After addition of Ni (NO₃)₂·6H₂O and Al (NO₃)₃·9H₂O to the ultrasonically dispersed g-C₃N₄ nanosheets, Ni²⁺ and Al³⁺ metal ions from the metal salts can be strongly bound onto the surface of negatively charged g-C₃N₄ nanosheets by electrostatic interactions. When urea and ammonium fluoride are added to the dispersion, a large amount of nuclei form and NiAl-LDH platelets grow onto the surface of g-C₃N₄ nanosheets under subsequent hydrothermal treatment. In this process, negatively charged g-C₃N₄ nanosheets could serve as nucleation sites for the *in situ* growth of NiAl-LDH sheets. As a result, restacking process of LDH sheets can be arrested effectively which leads to the 2D/2D assembly of g-C₃N₄ and NiAl-LDH sheets.^{42,43} Moreover, zeta potential measurements were also conducted (in water) to investigate the interactions between these two semiconductors (**Figure S1**). A significant shift in the zeta potential of g-C₃N₄ was observed after the formation of nanocomposite with NiAl-LDH, which clearly indicates that the g-C₃N₄/NiAl-LDH nanocomposites could self-assemble through electrostatic interactions.

TGA analysis was performed to confirm the contents of NiAl-LDH in the synthesized g-C₃N₄/NiAl-LDH nanocomposites under N₂ atmosphere at a heating rate of 10 °C min⁻¹. As can be seen in **Figure S2**, the bare NiAl-LDH exhibits two significant weight loss regions. The first weight loss from 25 to 200 °C can be assigned to the evaporation of surface adsorbed and interlayer water molecules, while the second weight loss at temperature between 250 and 350 °C

1
2
3 corresponds to the decomposition of the interlayer nitrate anions and de-hydroxylation of the
4
5 brucite-like layers.⁴⁴⁻⁴⁶ Besides, pure g-C₃N₄ decomposition starts at 550 °C and is completed at
6
7 ~700 °C, which correspond to the burning of g-C₃N₄.¹⁹ The general trend of thermal degradation
8
9 of g-C₃N₄/NiAl-LDH samples is similar to bare NiAl-LDH and g-C₃N₄. However, when
10
11 compared to bare NiAl-LDH, poor weight loss was observed over low temperature regions for g-
12
13 C₃N₄/NiAl-LDH samples, which might be due to the scarcity of interlayer water molecules and
14
15 nitrate anions owing to the self-exfoliation of LDH layers on g-C₃N₄ surface in the *in-situ*
16
17 synthesis process. Regardless, the content of NiAl-LDH can be confirmed using the weight
18
19 remainder after heating the samples over 800 °C. Therefore, the specific weight percentages of
20
21 NiAl-LDH in the nanocomposites were found to be 4.2, 9.7, 13.8 and 18.5%, for CNLDH-5,
22
23 CNLDH-10, CNLDH-15 and CNLDH-20, respectively.
24
25
26
27

28
29 The phase structure of the synthesized samples was investigated by XRD, and the results are
30
31 displayed in **Figure 1**. The pure g-C₃N₄ material has two diffraction peaks at about 27.8° and
32
33 13.23° corresponding to the characteristic interlayer stacking of the conjugated aromatic systems
34
35 and the in-planar structural repeating unit, respectively.³⁷ For pure NiAl-LDH, the reflections at
36
37 11.72°, 23.41°, 35.13°, 39.56°, 46.92°, 61.01°, and 62.43° are ascribed to the (003), (006), (012),
38
39 (015), (018), (110), and (113) lattice planes, which can be indexed to the hexagonal NiAl-LDH
40
41 (JCPDF22-0452). In the case of g-C₃N₄/NiAl-LDH heterostructures, a superimposition XRD
42
43 pattern of g-C₃N₄ and NiAl-LDH is observed, and with the increase in NiAl-LDH content, the
44
45 diffraction peaks of NiAl-LDH intensify gradually at the expense of g-C₃N₄ peaks, reflecting
46
47 their respective contents in the g-C₃N₄/NiAl-LDH heterostructures. Moreover, after introduction
48
49 of NiAl-LDH, the main peak of g-C₃N₄ (27.8°) in g-C₃N₄/NiAl-LDH composites slightly shifted
50
51
52
53
54
55
56
57
58
59
60

1
2
3 from the original position and appeared with decreased intensities, which clearly indicates the
4 coordination between the g-C₃N₄ and NiAl-LDH in g-C₃N₄/NiAl-LDH nanocomposites.
5
6

7
8 UV-vis DRS was performed to investigate the light response property of the synthesized
9 photocatalysts, since the photocatalytic activity is relevant to the optical absorption
10 characteristics. As shown in **Figure 2**, pure g-C₃N₄ displays a strong absorption edge located at
11 460 nm which corresponds to a band gap of ca. 2.7 eV. Bare NiAl-LDH exhibits mainly three
12 absorption bands in the UV and visible-light regions, in which the first one is located from 200 to
13 300 nm, second one from 300 to 500 nm, and the third one from 600 to 800 nm. The intrinsic
14 absorption band in the UV region (200 to 300 nm) could be assigned to ligand-to-metal charge
15 transfer (LMCT) from the O 2p orbital to the Ni 3d t_{2g} orbital, while the bands from 300 to 800
16 nm are corresponding to d-d transitions, which are characteristics of Ni²⁺ ions in an octahedral
17 geometry.^{47,48} The absorption bands at 380 and 740 nm are attributed to spin-allowed transitions
18 $^3A_{2g}(F) \rightarrow ^3T_{1g}(P)$ and $^3A_{2g}(F) \rightarrow ^3T_{1g}(F)$, respectively, resulting from d⁸ configuration of Ni²⁺
19 ions in an octahedral field. The other bands located at 420 and 645 nm are attributed to spin-
20 forbidden transitions $^3A_{2g}(F) \rightarrow ^1T_{2g}(D)$ and $^3A_{2g}(F) \rightarrow ^1E_g(D)$, respectively.^{49,50} A slight blue
21 shift in the absorption edge was observed after the introduction of NiAl-LDH on g-C₃N₄, and
22 with increasing NiAl-LDH content, the absorption edge was seen to shift towards the lower
23 wavelength region. A similar kind of blue shift in the absorption edge is also observed in
24 previous reports.^{20,51} More remarkably, with an increase in the weight percentage of the NiAl-
25 LDH on g-C₃N₄, a decrease in light absorption in the UV region (300 to 400 nm) and increase in
26 the light absorption in the visible region (550 to 800 nm) was observed, which could be
27 attributed to the strong interaction between g-C₃N₄ and NiAl-LDH in the resulting composites.
28
29 The improved light absorption in the visible region can therefore provide more photogenerated
30
31
32
33
34
35
36
37
38
39
40
41
42
43
44
45
46
47
48
49
50
51
52
53
54
55
56
57
58
59
60

1
2
3 charge carriers required for the photocatalytic reactions, which can result in enhanced
4 photocatalytic properties.
5
6

7
8 **Figure 3** displays the FT-IR patterns of the synthesized g-C₃N₄, NiAl-LDH and g-C₃N₄/NiAl-
9 LDH nanocomposites. For g-C₃N₄, the sharp and intense band at 805 cm⁻¹ corresponds to the
10 characteristic breathing mode of the s-triazine ring system, and the broad band at around 3200
11 cm⁻¹ corresponds to the stretching vibrational modes of residual N–H components associated
12 with uncondensed amino groups. Additionally, several bands in the 1200–1650 cm⁻¹ region are
13 assigned to the typical stretching modes of aromatic C–N heterocycles.³⁷ The bands at 3480 and
14 1635 cm⁻¹ in the NiAl-LDH spectrum can be assigned to the O–H stretching and bending
15 vibrations, respectively, and the strong band at 1365 cm⁻¹ can be assigned to the bending
16 vibrations of NO₃⁻ ions intercalated in the lamellar structure.⁴⁶ The other bands below 800 cm⁻¹
17 are attributed to the translational modes of metal–oxygen (Ni–O and Al–O) and
18 metal–oxygen–metal (Ni–O–Al) bands.^{52,53} It should be noted that the FT-IR spectra of g-
19 C₃N₄/NiAl-LDH composites consists of all the characteristic bands of g-C₃N₄ along with the
20 broad shoulder band at 3480 cm⁻¹, which originates from the stretching vibrations of O–H
21 groups existing in NiAl-LDH. Moreover, after the addition of NiAl-LDH, the bands at 885 cm⁻¹
22 showed a blue shift, which is consistent with the UV-vis DRS observations. These results clearly
23 demonstrate the effect and existence of NiAl-LDH on g-C₃N₄ through the interfacial electrostatic
24 interactions. Such strong interactions between the semiconductors are clearly of significance to
25 the charge transfer and can induce a synergistic effect to enhance the photocatalytic activity.
26
27
28
29
30
31
32
33
34
35
36
37
38
39
40
41
42
43
44
45
46
47
48

49 The morphologies and microstructures of pure g-C₃N₄, NiAl-LDH and g-C₃N₄/NiAl-LDH
50 nanocomposites were investigated by TEM and HR-TEM. The TEM image of pure NiAl-LDH
51 (**Figure 4a**) exhibits 3D flower-like morphology consisting of plenty of ultrathin nanoflakes. As
52
53
54
55
56
57
58
59
60

1
2
3 expected, g-C₃N₄ possessed a 2D sheet-like structure with irregular orientation (**Figure 4b**),
4 which indicates the successful exfoliation of bulk g-C₃N₄. Interestingly, in the case of g-
5 C₃N₄/NiAl-LDH nanocomposites (CNLDH-10), the flower-like morphology of NiAl-LDH
6 disappears; however, a number of ultrathin 2D LDH sheets are well grown on the surface of g-
7 C₃N₄, which demonstrates the successful self-assembly of g-C₃N₄ and NiAl-LDH by electrostatic
8 interactions (**Figures 4c – e**). This clearly indicates that, during the *in situ* growth process both g-
9 C₃N₄ and NiAl-LDH nanosheets strongly interact with each other due to their opposite
10 surface charges and these interactions subsequently contribute to avoid the restacking of NiAl-
11 LDH nanosheets in the nanocomposite samples. Besides, the HR-TEM image (**Figure 4f**)
12 exhibits lattice fringes corresponding to the interplanar distance of 0.32 and 0.26 nm, which can
13 be ascribed to the (002) plane of g-C₃N₄ and (012) plane of NiAl-LDH, respectively.^{35,54}
14 Additionally, EDS elemental mapping images (**Figure S3**) further confirm that the g-C₃N₄/NiAl-
15 LDH heterojunction (CNLDH-10) was composed of C, N, Ni, Al and O elements. The
16 homogenous distribution of the component elements in the CNLDH-10 heterojunction clearly
17 demonstrates that both g-C₃N₄ and NiAl-LDH phases are indeed fully mixed and intimately
18 contacted, rather than existing as separate aggregates in the CNLDH-10 heterojunction.
19
20
21
22
23
24
25
26
27
28
29
30
31
32
33
34
35
36
37
38
39

40 The XPS spectra were conducted to analyze the detailed chemical status of the pure and
41 composite photocatalysts. As observed from **Figure S4**, the survey XPS spectrum of the
42 CNLDH-10 sample exhibits the peaks corresponds to C, N, Ni, Al, and O elements, revealing the
43 presence of g-C₃N₄ and NiAl-LDH in the composite. For pure g-C₃N₄, the N 1s spectrum can be
44 deconvoluted into three peaks located at the binding energies of 398.4, 399.6, and 400.9 eV,
45 which are ascribed to sp² hybridized nitrogen in triazine rings (C–N=C), bridged tertiary
46 nitrogen N–(C)₃ groups, and amino functional groups (N–H), respectively (**Figure 5a**). The C 1s
47
48
49
50
51
52
53
54
55
56
57
58
59
60

1
2
3 spectrum in **Figure 5b** can be fitted by two peaks, attributed to C–C at 284.5 eV and N=C–N at
4 288.1 eV.^{16,54} Besides, the Ni 2p spectrum (**Figure 5c**) for pure NiAl-LDH consists of two peaks
5 with the binding energies of 856.2 and 873.8 eV, corresponding to Ni 2p_{3/2} and Ni 2p_{1/2},
6 respectively, in agreement with the Ni²⁺ oxidation state, and the additional satellite peaks
7 indicate the presence of a high-spin divalent state of Ni²⁺ in the sample.^{55,56} Additionally, the
8 high resolution Al 2p spectrum (**Figure 5d**) confirms the Al³⁺ oxidation state in the pure NiAl-
9 LDH.⁵⁷ For the g-C₃N₄/NiAl-LDH nanocomposites, a significant increase in the binding energies
10 of Ni 2p_{3/2} and Ni 2p_{1/2}, and a small decrease in the C 1s binding energy were observed
11 compared to the pure reference materials. However, no such shift in the binding energies of N 1s
12 and Al 2p were observed for the pure and composite samples. The increased and decreased
13 binding energies of Ni 2p and C 1s suggesting the strong electron transfer between g-C₃N₄ and
14 NiAl-LDH, and the similar phenomenon was also observed in previous reports.^{36,58}

3.2. Photocatalytic CO₂ Reduction Activities of the g-C₃N₄/NiAl-LDH Heterojunctions.

31
32 The photocatalytic activities of all synthesized g-C₃N₄/NiAl-LDH photocatalysts, including pure
33 g-C₃N₄ and NiAl-LDH were evaluated under visible-light illumination and the results are
34 displayed in **Figure 6**. Carbon monoxide was found to be the main and direct product of CO₂
35 reduction reaction and no other carbonaceous products were observed. However, other products
36 such as H₂ and O₂, which are generated from the water (vapor) splitting, were also detected.
37 During the evaluation of photocatalysts, controlled experiments in the absence of light irradiation
38 or catalysts were also conducted, and the results revealed that no reduced products could be
39 detected, illustrating that light irradiation and photocatalysts are essential for photocatalytic CO₂
40 reduction reactions. Moreover, neither CO, nor other products can be detected by introducing
41 CO₂ into the reaction system without water vapor or introducing N₂ instead of CO₂ into the
42
43
44
45
46
47
48
49
50
51
52
53
54
55
56
57
58
59
60

1
2
3 reaction system under light irradiation, clearly demonstrating that CO was solely originated by
4 the reduction of CO₂ with water vapor over the photocatalysts under the visible-light
5 illumination.
6
7
8
9

10 **Figure 6a** shows the evolution of CO as a function of illumination time on all the synthesized
11 photocatalysts under visible-light irradiation. As expected, pure g-C₃N₄ exhibited a minimal
12 generation of CO, attaining a total yield of 0.39 μmol for 5 h, due to rapid recombination of
13 photogenerated charge carriers. Moreover, in this photocatalytic process g-C₃N₄ also generated
14 significant amounts of H₂ and O₂ through water (vapor) splitting owing to its suitable band edge
15 potentials for both the water reduction and oxidation reactions. Besides, pure NiAl-LDH exhibits
16 a low photocatalytic activity for CO₂ reduction, in which the amount of generated CO is only
17 0.23 μmol for 5 h.
18
19
20
21
22
23
24
25
26
27

28 Importantly, after forming the 2D/2D heterostructure of g-C₃N₄ with NiAl-LDH, the obtained
29 g-C₃N₄/NiAl-LDH photocatalysts exhibited remarkable photocatalytic activity for CO evolution.
30
31 As shown in **Figure S5**, the rate of CO evolution increased with increasing the NiAl-LDH
32 content in the g-C₃N₄/NiAl-LDH nanocomposites, reaching a highest rate of 8.2 μmol h⁻¹g⁻¹ for
33 the case of NiAl-LDH content of 10 wt.% (CNLDH-10), which is more than five times that for
34 pure g-C₃N₄ (1.56 μmol h⁻¹g⁻¹) and almost nine times higher than that for NiAl-LDH (0.92 μmol
35 h⁻¹g⁻¹). Notably, the CO selectivity for CNLDH-10 photocatalyst is almost 82%. As shown in
36
37
38
39
40
41
42
43
44 **Figure 6b** and **c**, the synthesized composites not only exhibited remarkable enhancement in the
45 generation of CO but also exhibited significant enhancement in the generation of H₂ and O₂. It is
46 also worth noting that all the samples displayed (CO + H₂):O₂ products stoichiometry close to
47 2:1, since both CO₂ reduction to CO, and H₂O reduction to H₂ are 2e⁻ processes, whereas H₂O
48 oxidation is a 4e⁻ process. However, when the NiAl-LDH content increased beyond its optimum
49
50
51
52
53
54
55
56
57

1
2
3 level (~10 wt.%) in the g-C₃N₄/NiAl-LDH composites, a decrease in the reduction products rate
4 was observed. This can probably be attributed to the following reasons: (1) excessive amount of
5 NiAl-LDH may cover the active sites on the surface of g-C₃N₄, and (2) at a very high content of
6 NiAl-LDH, there is a good chance of the development overlapped (self-aggregated) NiAl-LDH
7 sheets in the sample which reduces the density of g-C₃N₄/NiAl-LDH heterojunctions. Hence, an
8 optimized content of NiAl-LDH is crucial for optimizing the photocatalytic activity of g-
9 C₃N₄/NiAl-LDH composites.

19 The impact of surface area on CO₂ photoreduction activities of all the samples was
20 investigated using nitrogen adsorption-desorption measurements. As can be seen **Figure S6**, pure
21 g-C₃N₄ nanosheets possesses higher specific surface area ($S_{\text{BET}} = 106.9 \text{ m}^2/\text{g}$) in comparison with
22 NiAl-LDH ($S_{\text{BET}} = 28.5 \text{ m}^2/\text{g}$) and also the higher CO₂ photoreduction activity. It was found that
23 when NiAl-LDH introduced into g-C₃N₄ nanosheets, the specific surface areas of g-C₃N₄/NiAl-
24 LDH composites were similar to that of g-C₃N₄, but their CO₂ photoreduction activities are
25 apparently different. This clearly demonstrates that there should be another key factor other than
26 surface area that influences the CO₂ photoreduction activities of the present nanocomposites
27 significantly. As such, the variation in the photoreduction activities of these nanocomposites is
28 mainly rely on the efficient separation of photogenerated electron-hole pairs which resulted by
29 the intimate interface between g-C₃N₄ and NiAl-LDH. This is further investigated by the CO₂
30 photoreduction results of a physical mixture of g-C₃N₄ and NiAl-LDH (denoted as CNLDH-10
31 PM in **Figure 6a**, b, and c). Clearly, physically mixed CNLDH-10 PM (10 wt% NiAl-LDH on g-
32 C₃N₄) composite showed poor CO evolution activity ($2.84 \mu\text{mol h}^{-1}\text{g}^{-1}$), indicating the absence
33 of strong electrostatic interactions between the g-C₃N₄ and NiAl-LDH.

1
2
3 Additionally, the photocatalytic activity of the presented 2D/2D system was also compared
4 with the commercial P25 reference catalyst, which showed rather negligible photocatalytic CO
5 evolution due to the rapid charge carrier recombination, low CO₂ absorptivity, and improper
6 conduction band (CB) potential to drive CO₂ reduction.³⁶ Notably, the photocatalytic CO
7 evolution activity of the CNLDH-10 composite is also higher than the various g-C₃N₄-based
8 photocatalysts reported previously, such as g-C₃N₄/BiOBr/Au,⁵⁹ BiOI/g-C₃N₄,⁶⁰ g-C₃N₄/C,⁶¹ g-
9 C₃N₄/Bi₂WO₆,⁶² and other photocatalysts, for example rGO-Ag-CdS,⁶³ I-TiO₂,⁶⁴ PbS
10 QD's/Cu/TiO₂,⁶⁵ Au@SrTiO₃,⁶⁶ and so on.

11
12 Furthermore, **Figure 6d** displays an action spectrum of CNLDH-10 catalyst, which exhibits
13 the wavelength-dependent AQY values on account of CO production using appropriate band-
14 pass filters. It can be seen that the AQY values of CO production are essentially dependent on
15 the incident wavelength that matches well with the absorption in the optical spectrum of the
16 CNLDH-10 catalyst. Moreover, action spectrum reveals higher AQY values in the 400-450 nm
17 wavelength regions; whereas very low AQY values observed after the wavelength of 500 nm.
18 These results clearly indicate that the inter-band transitions of g-C₃N₄ predominantly lead to the
19 CO₂ photoreduction of the CNLDH-10 catalyst. The significant AQY values obtained in this
20 study are 0.39% at 400 nm, and 0.21% at 420 nm, respectively. Notably, the AQY values of the
21 present system at 400 and 420 nm are indeed higher than the other state of the art CO₂ reduction
22 photocatalysts.⁶⁷⁻⁷⁰

23
24 Reusability and stability are critical issues for the long-term use of a photocatalyst in practical
25 applications. In order to investigate the photostability of the synthesized g-C₃N₄/NiAl-LDH
26 nanocomposites, four cycling CO₂ photocatalytic reduction experiments were performed over
27 CNLDH-10 under the same experimental conditions. Each run was conducted with the periodic
28
29
30
31
32
33
34
35
36
37
38
39
40
41
42
43
44
45
46
47
48
49
50
51
52
53
54
55
56
57
58
59
60

1
2
3 replacement of fresh CO₂ and water vapor. As shown in **Figure 7**, the photocatalytic CO
4 evolution of CNLDH-10 was decreased to 1.79 μmol after four successive experimental runs
5 (~20 h), retaining over 86% of its original activity (2.05 μmol) under the visible-light irradiation.
6
7
8 A slight depletion in the activity may originate from the inevitable loss of the catalyst during the
9 recycling runs. The results indicate that LDH was firmly attached to the g-C₃N₄ substrate during
10 the *in situ* synthetic process, owing to their opposite surface charges. Subsequently,
11 immobilization of LDH on g-C₃N₄ surface can not only enhance the photocatalytic CO₂ reduction
12 performance, but also improves the stability of the catalyst during the photocatalytic
13 reactions.^{33,71} **Figure S7** shows a comparison of the XRD patterns of CNLDH-10 sample before
14 and after the photocatalytic reaction and no obvious peak change in the XRD patterns was
15 observed, suggesting the structural stability of the composites during the photocatalytic reaction
16 process. Moreover, the TEM image (**Figure S7**) of the reused sample also clearly demonstrated
17 that the morphology of the CCG-10 photocatalyst did not change significantly after the reaction.
18
19
20
21
22
23
24
25
26
27
28
29
30
31
32

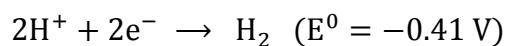
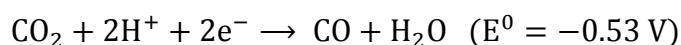
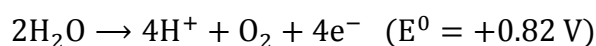
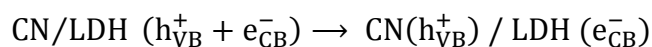
33 **3.3. Photocatalytic Mechanism in the g-C₃N₄/NiAl-LDH Heterojunction System.** In order
34 to investigate the photocatalytic mechanism for the enhanced photocatalytic CO₂ reduction by
35 the g-C₃N₄/NiAl-LDH heterojunctions, PL spectra of the photocatalysts were recorded. As
36 shown in **Figure 8a**, all the photocatalysts show a broad PL emission peak centered at around
37 460 nm, which corresponds to the band-band PL due to the recombination of photogenerated
38 charge carriers of g-C₃N₄. It can be found that the PL emission intensities reach the maximum
39 value for pure g-C₃N₄ and decrease significantly with the introduction of NiAl-LDH, clearly
40 demonstrating that the recombination of the photogenerated electron-hole pairs in g-C₃N₄ has
41 been effectively inhibited after the heterojunction formation with NiAl-LDH. The CNLDH-10
42
43
44
45
46
47
48
49
50
51
52
53
54
55
56
57
58
59
60

1
2
3 sample exhibits the least PL emission intensity i.e., the lowest recombination rate, which agrees
4 well with its highest photocatalytic activity as mentioned above.
5
6

7
8 To provide further evidence to support the efficient photogenerated charge carriers separation
9 of the present system, photoelectrochemical measurements were performed. **Figure 8b** shows
10 reproducible and stable photocurrent responses to on-off cycles in the pure and composite
11 samples. Notably, the CNLDH-10 photocatalyst exhibited the highest photocurrent response in
12 comparison with those of pure g-C₃N₄ and NiAl-LDH, which can be attributed to the existence
13 of a strong interface between g-C₃N₄ and NiAl-LDH, where photogenerated charge carriers
14 could be efficiently separated. The greater transfer efficiency of charge carriers lead to the
15 remarkable photocatalytic activity of g-C₃N₄/NiAl-LDH nanocomposites.
16
17
18
19
20
21
22
23
24
25

26 In addition, the valence band (VB) and CB positions of g-C₃N₄ and NiAl-LDH were
27 investigated by valence band XPS (VB-XPS). As shown in **Figure 9**, the VB edge positions of g-
28 C₃N₄ and NiAl-LDH are determined to be 1.38 and 1.62 eV, respectively. Based on the band
29 gaps of g-C₃N₄ (2.7 eV) and NiAl-LDH (2.32 eV), the CB edge positions are calculated to be
30 -1.32 eV and -0.7 eV for g-C₃N₄ and NiAl-LDH, respectively. Therefore, it could be concluded
31 that the CB minimum of NiAl-LDH is lower than that of g-C₃N₄, while the VB maximum of g-
32 C₃N₄ is higher than that of NiAl-LDH. Based on the above results, the photocatalytic mechanism
33 for the g-C₃N₄/NiAl-LDH nanocomposites is proposed and schematically illustrated in
34 **Figure 10**. Upon visible-light irradiation, both g-C₃N₄ and NiAl-LDH can be excited to generate
35 the electrons and holes in CB and VB, respectively, since their band gap energies lie in the
36 visible region. The excited electrons on the CB of g-C₃N₄ could pass across the heterojunction
37 into the CB of NiAl-LDH, while the formed holes on the VB of NiAl-LDH can pass through the
38 heterojunction into the VB of g-C₃N₄. Such promoted charge separation or suppressed charge
39
40
41
42
43
44
45
46
47
48
49
50
51
52
53
54
55
56
57
58
59
60

recombination results in mutual activation of both g-C₃N₄ and NiAl-LDH. The resultant holes in the VB of g-C₃N₄ and those transferred from the VB of NiAl-LDH can oxidize the chemisorbed water molecules on the surface of g-C₃N₄ to generate O₂ and protons. At the same time, the enriched electrons on the CB of NiAl-LDH could be trapped by the CO₂ to generate CO under the assistance of the protons, as explained by the following equations.



4. CONCLUSIONS

In summary, g-C₃N₄/NiAl-LDH heterojunctions were synthesized by an *in situ* hydrothermal method which established a strong interface system due to the 2D/2D assembly of positively charged NiAl-LDH sheets and negatively charged g-C₃N₄ nanosheets. The resulting 2D/2D g-C₃N₄/NiAl-LDH heterojunctions exhibited excellent performance for photocatalytic CO₂ reduction under visible-light irradiation. The optimum g-C₃N₄/NiAl-LDH heterojunctions showed the highest CO production rate of 8.2 μmol h⁻¹g⁻¹, which is 5 times higher than that of pure g-C₃N₄ and 9 times higher than that for pure NiAl-LDH. The high performance of this new 2D/2D composite material is ascribed mainly to the synergistic effect between g-C₃N₄ and NiAl-LDH, including strong interfacial contact due to 2D/2D assembly, suppressed recombination, improved separation, and efficient transfer of excited charge carriers. More importantly, the heterojunctions were highly photostable even after successive experimental runs, without any obvious change in the activity.

ASSOCIATED CONTENT

Supporting Information

Zeta potential measurements; TGA spectra; EDS spectrum and corresponding elemental mapping images; XPS survey spectrum; Photocatalytic CO, H₂ and O₂ evolution rates graph; N₂ adsorption–desorption isotherms; TEM and XRD of fresh and reused photocatalyst.

ACKNOWLEDGEMENTS

S. T. likes to thank the Director, IISER Pune, for funding postdoctoral fellowship. SBO acknowledges funding support by DST Nanomission Thematic Unit program “Nanoscience for Clean Energy). The authors also like to acknowledge Reshma Bhosale and Aparna Deshpande for critical reading of the manuscript.

REFERENCES

- (1) Kubacka, A.; Fernández-García, M.; Colón, G. Advanced Nanoarchitectures for Solar Photocatalytic Applications. *Chem. Rev.* **2012**, *112* (3), 1555–1614.
- (2) Goeppert, A.; Czaun, M.; Jones, J. P.; Surya Prakash, G. K.; Olah, G. A., Recycling of Carbon Dioxide to Methanol and Derived Products – Closing the Loop. *Chem. Soc. Rev.* **2014**, *43*, 7995–8048.
- (3) Herron, J. A.; Kim, J.; Upadhye, A. A.; Huber, G. W.; Maravelias, C. T. A General Framework for the Assessment of Solar Fuel Technologies. *Energy Environ. Sci.* **2015**, *8*, 126–157.
- (4) Zhu, D. D.; Liu, J. L.; Qiao, S. Z. Recent Advances in Inorganic Heterogeneous Electrocatalysts for Reduction of Carbon Dioxide. *Adv. Mater.* **2016**, *28*, 3423–3452.
- (5) Kondratenko, E. V.; Mul, G.; Baltrusaitis, J.; Larrazábal, G. O.; Pérez-Ramírez, J. Status and Perspectives of CO₂ Conversion into Fuels and Chemicals by Catalytic, Photocatalytic and Electrocatalytic Processes. *Energy Environ. Sci.* **2013**, *6*, 3112–3135.
- (6) Inoue, T.; Fujishima, A.; Konishi, S.; Honda, K. Photoelectrocatalytic Reduction of Carbon Dioxide in Aqueous Suspensions of Semiconductor Powders. *Nature* **1979**, *277*, 637–638.

- 1
2
3 (7) Yu, J.; Qi, L.; Jaroniec, M. Hydrogen Production by Photocatalytic Water Splitting over
4 Pt/TiO₂ Nanosheets with Exposed (001) Facets. *J. Phys. Chem. C* **2010**, *114*, 13118–13125.
5
6 (8) Sheikh, A.; Yengantiwar, A.; Deo, M.; Kelkar, S.; Ogale, S. B. Nearfield Plasmonic
7 Functionalization of Light Harvesting Oxide–Oxide Heterojunctions for Efficient Solar
8 Photoelectrochemical Water Splitting: The AuNP/ZnFe₂O₄/ZnO System. *Small* **2013**, *9*,
9 2091–2096.
10
11 (9) Wang, G.; Huang, B.; Li, Z.; Lou, Z.; Wang, Z.; Dai, Y.; Whangbo, M. H. Synthesis and
12 Characterization of ZnS with Controlled Amount of S Vacancies for Photocatalytic H₂
13 Production under Visible Light. *Sci. Rep.* **2015**, *5*, 8544.
14
15 (10) Bhosale, R.; Kelkar, S.; Parte, G.; Fernandes, R.; Kothari, D. C.; Ogale, S. B. NiS₁₉₇: A
16 New Efficient Water Oxidation Catalyst for Photoelectrochemical Hydrogen Generation.
17 *ACS Appl. Mater. Interfaces* **2015**, *7*, 20053–20060.
18
19 (11) Higashi, M.; Domen, K.; Abe, R. Highly Stable Water Splitting on Oxynitride TaON
20 Photoanode System under Visible Light Irradiation. *J. Am. Chem. Soc.* **2012**, *134*,
21 6968–6971.
22
23 (12) Wang, X.; Maeda, K.; Thomas, A.; Takane, K.; Xin, G.; Carlsson, J. M.; Domen, K.;
24 Antonietti, M. A Metal-Free Polymeric Photocatalyst for Hydrogen Production from Water
25 under Visible Light. *Nat. Mater.* **2009**, *8*, 76–80.
26
27 (13) Ong, W. J.; Tan, L. L.; Ng, Y. H.; Yong, S. T.; Chai, S. P. Graphitic Carbon Nitride (g-
28 C₃N₄)-Based Photocatalysts for Artificial Photosynthesis and Environmental Remediation:
29 Are We a Step Closer To Achieving Sustainability?. *Chem. Rev.* **2016**, *116* (12), 7159–
30 7329.
31
32 (14) Suryawanshi, A.; Dhanasekaran, P.; Mhamane, D.; Kelkar, S.; Patil, S.; Gupta, N.; Ogale,
33 S. B. Doubling of Photocatalytic H₂ Evolution from g-C₃N₄ via Its Nanocomposite
34 Formation with Multiwall Carbon Nanotubes: Electronic and Morphological Effects. *Int. J.*
35 *Hydrogen Energy* **2012**, *37*, 9584–9589.
36
37 (15) Wang, K.; Li, Q.; Liu, B.; Cheng, B.; Hob, W.; Yu, J. Sulfur-Doped g-C₃N₄ with Enhanced
38 Photocatalytic CO₂-Reduction Performance. *Appl. Catal. B* **2015**, *176–177*, 44–52.
39
40 (16) Li, X.; Hartley, G.; Ward, A. J.; Young, P.; Masters, A. F.; Maschmeyer, T. Hydrogenated
41 Defects in Graphitic Carbon Nitride Nanosheets for Improved Photocatalytic Hydrogen
42 Evolution. *J. Phys. Chem. C* **2015**, *119* (27), 14938–14946.
43
44
45
46
47
48
49
50
51
52
53
54
55
56
57
58
59
60

- 1
2
3
4
5
6
7
8
9
10
11
12
13
14
15
16
17
18
19
20
21
22
23
24
25
26
27
28
29
30
31
32
33
34
35
36
37
38
39
40
41
42
43
44
45
46
47
48
49
50
51
52
53
54
55
56
57
58
59
60
- (17) Ong, W. J.; Tan, L. L.; Chai, S. P.; Yong, S. T. Graphene Oxide as a Structure-Directing Agent for the Two-Dimensional Interface Engineering of Sandwich-Like Graphene-g-C₃N₄ Hybrid Nanostructures with Enhanced Visible-Light Photoreduction of CO₂ to Methane. *Chem. Commun.* **2015**, *51*, 858–861.
- (18) Tonda, S.; Kumar, S.; Shanker, V. In Situ Growth Strategy for Highly Efficient Ag₂CO₃/g-C₃N₄ Hetero/Nanojunctions with Enhanced Photocatalytic Activity under Sunlight Irradiation. *J. Environ. Chem. Engg.* **2015**, *3*, 852–861.
- (19) Kumar, S.; Surendar, T.; Baruah, A. Shanker, V. Synthesis of a Novel and Stable g-C₃N₄-Ag₃PO₄ Hybrid Nanocomposite Photocatalyst and Study of the Photocatalytic Activity under Visible Light Irradiation. *J. Mater. Chem. A* **2013**, *1*, 5333–5340.
- (20) Nayak, S.; Mohapatra, L.; Parida, K. Visible Light-Driven Novel g-C₃N₄/NiFe-LDH Composite Photocatalyst with Enhanced Photocatalytic Activity towards Water Oxidation and Reduction Reaction. *J. Mater. Chem. A* **2015**, *3*, 18622–18635.
- (21) He, Y.; Wang, Y.; Zhang, L.; Teng, B.; Fan, M. High-Efficiency Conversion of CO₂ to Fuel over ZnO/g-C₃N₄ Photocatalyst. *Appl. Catal. B* **2015**, *168-169*, 1–8.
- (22) Ong, W. J.; Tan, L. L.; Chai, S. P.; Yong, S. T. Heterojunction Engineering of Graphitic Carbon Nitride (g-C₃N₄) via Pt Loading with Improved Daylight-Induced Photocatalytic Reduction of Carbon Dioxide to Methane. *Dalton Trans.* **2015**, *44*, 1249–1257.
- (23) Qin, J.; Huo, J.; Zhang, P.; Zeng, J.; Wang, T.; H. Zeng, Improving the Photocatalytic Hydrogen Production of Ag/g-C₃N₄ Nanocomposites by Dye-Sensitization under Visible Light Irradiation. *Nanoscale* **2016**, *8*, 2249–2259.
- (24) Gunjekar, J. L.; Kim, I. Y.; Lee, J. M.; Lee, N. S.; Hwang, S. J. Self-Assembly of Layered Double Hydroxide 2D Nanoplates with Graphene Nanosheets: An Effective Way to Improve the Photocatalytic Activity of 2D Nanostructured Materials for Visible Light-Induced O₂ Generation. *Energy Environ. Sci.* **2013**, *6*, 1008–1017.
- (25) Hu, S. W.; Yang, L.W.; Tian, Y.; Wei, X. L.; Ding, J. W.; Zhong, J. X.; Chu, P. K. Non-Covalent Doping of Graphitic Carbon Nitride with Ultrathin Graphene Oxide and Molybdenum Disulfide Nanosheets: An Effective Binary Heterojunction Photocatalyst under Visible Light Irradiation. *J. Colloid Interface Sci.* **2014**, *431*, 42–49.
- (26) Zhang, G.; Zang, S.; Wang, X. Layered Co(OH)₂ Deposited Polymeric Carbon Nitriles for Photocatalytic Water Oxidation. *ACS Catal.* **2015**, *5*, 941–947.

- 1
2
3 (27) Hou, Y.; Wen, Z.; Cui, S.; Guo, X.; Chen, J. Constructing 2D Porous Graphitic C₃N₄
4 Nanosheets/Nitrogen-Doped Graphene/Layered MoS₂ Ternary Nanojunction with
5 Enhanced Photoelectrochemical Activity. *Adv. Mater.* **2013**, *25*, 6291–6297.
6
7
8 (28) Xiang, Q.; Yu, J.; Jaroniec, M. Preparation and Enhanced Visible-Light Photocatalytic H₂-
9 Production Activity of Graphene/C₃N₄ Composites. *J. Phys. Chem. C* **2011**, *115*, 7355–
10 7363.
11
12
13 (29) Liu, H.; Zhang, Z.; Meng, J.; Zhang, J. Novel Visible-Light-Driven CdIn₂S₄/Mesoporous
14 g-C₃N₄ Hybrids for Efficient Photocatalytic Reduction of CO₂ to Methanol. *J. Mol. Catal.*
15 *A: Chem.* **2017**, *430*, 9–19.
16
17
18 (30) Wang Q.; O’Hare, D. Recent Advances in the Synthesis and Application of Layered
19 Double Hydroxide (LDH) Nanosheets. *Chem. Rev.* **2012**, *112*, 4124–4155.
20
21
22 (31) Zhao, Y.; Jia, X.; Waterhouse, G. I. N.; Wu, L. Z.; Tung, C. H.; O’Hare, D.; Zhang, T.
23 Layered Double Hydroxide Nanostructured Photocatalysts for Renewable Energy
24 Production. *Adv. Energy Mater.* **2016**, *6* (6), 1501974.
25
26
27 (32) Zhang, L.; Ou, M.; Yao, H.; Li, Z.; Qu, D.; Liu, F.; Wang, J.; Wang, J.; Li, Z. Enhanced
28 Supercapacitive Performance of Graphite-Like C₃N₄ Assembled with NiAl-Layered
29 Double Hydroxide. *Electrochim. Acta* **2015**, *186*, 292–301.
30
31
32 (33) Xue, L.; Cheng, Y.; Sun, X.; Zhou, Z.; Xiao, X.; Hu, Z.; Liu, X. The Formation
33 Mechanism and Photocatalytic Activity of Hierarchical NiAl-LDH Films on an Al
34 Substrate Prepared under Acidic Conditions. *Chem. Commun.* **2014**, *50*, 2301-2303.
35
36
37 (34) Sun, Y.; Zhou, J.; Cai, W.; Zhao, R.; Yuan, J. Hierarchically Porous NiAl-LDH
38 Nanoparticles as Highly Efficient Adsorbent for p-Nitrophenol from Water. *Appl. Surf.*
39 *Sci.* **2015**, *349*, 897–903.
40
41
42 (35) Li, M.; Zhu, J. E.; Zhang, L.; Chen, X.; Zhang, H.; Zhang, F.; Xu, S.; Evans, D. G. Facile
43 Synthesis of NiAl-Layered Double Hydroxide/Graphene Hybrid with Enhanced
44 Electrochemical Properties for Detection of Dopamine. *Nanoscale* **2011**, *3*, 4240-4246.
45
46
47 (36) Kumar, S.; Isaacs, M. A.; Trofimovaite, R.; Parlett, C. M. A.; Douthwaite, R. E.; Coulson,
48 B.; Cockett, M. C. R.; Wilson, K.; Lee, A. F. P25@CoAl Layered Double Hydroxide
49 Heterojunction Nanocomposites for CO₂ Photocatalytic Reduction. *Appl. Catal. B* **2017**,
50 *209*, 394–404.
51
52
53
54
55
56
57
58
59
60

- 1
2
3 (37) Tonda, S.; Kumar, S.; Kandula, S.; Shanker, V. Fe-Doped and -Mediated Graphitic Carbon
4 Nitride Nanosheets for Enhanced Photocatalytic Performance under Natural Sunlight. *J.*
5 *Mater. Chem. A* **2014**, *2*, 6772–6780.
6
7
8 (38) Du, Y. Y.; Jin, Q.; Feng, J. T.; Zhang, N.; He, Y. F.; Li, D. Q. Flower-Like Au/Ni–Al
9 Hydrotalcite with Hierarchical Pore Structure as a Multifunctional Catalyst for Catalytic
10 Oxidation of Alcohol. *Catal. Sci. Technol.* **2015**, *5*, 3216–3225.
11
12 (39) Liu, J.; Liu, Y.; Liu, N.; Han, Y.; Zhang, X.; Huang, H.; Lifshitz, Y.; Lee, S. T.; Zhong, J.;
13 Kang, Z. Metal-Free Efficient Photocatalyst for Stable Visible Water Splitting via a Two-
14 Electron Pathway. *Science* **2015**, *347*, 970–974.
15
16 (40) Luo, M.; Yao, W.; Huang, C.; Wu, Q.; Xu, Q. Shape Effects of Pt Nanoparticles on
17 Hydrogen Production *via* Pt/CdS Photocatalysts under Visible Light. *J. Mater. Chem. A*
18 **2015**, *3*, 13884–13891.
19
20 (41) Luo, M.; Lu, P.; Yao, W.; Huang, C.; Xu, Q.; Wu, Q.; Kuwahara, Y.; Yamashita, H. Shape
21 and Composition Effects on Photocatalytic Hydrogen Production for Pt–Pd Alloy
22 Cocatalysts. *ACS Appl. Mater. Interfaces*, **2016**, *8* (32), 20667–20674.
23
24 (42) Fang, J.; Li, M.; Li, Q.; Zhang, W.; Shou, Q.; Liu, F.; Zhang, X.; Cheng, J. Microwave-
25 Assisted Synthesis of CoAl-Layered Double Hydroxide/Graphene Oxide Composite and its
26 Application in Supercapacitors. *Electrochim. Acta* **2012**, *85*, 248–255.
27
28 (43) Gao, Z.; Wang, J.; Li, Z.; Yang, W.; Wang, B.; Hou, M.; He, Y.; Liu, Q.; Mann, T.; Yang,
29 P.; Zhang, M.; Liu, L. Graphene Nanosheet/Ni²⁺/Al³⁺ Layered Double-Hydroxide
30 Composite as a Novel Electrode for a Supercapacitor, *Chem. Mater.* **2011**, *23*, 3509–3516.
31
32 (44) Poul, L.; Jouini, N.; Fievet, F. Layered Hydroxide Metal Acetates (Metal = Zinc, Cobalt,
33 and Nickel): Elaboration *via* Hydrolysis in Polyol Medium and Comparative Study. *Chem.*
34 *Mater.* **2000**, *12*, 3123–3132.
35
36 (45) Woo, M. A.; Song, M. S.; Kim, T. W.; Kim, I. Y.; Ju, J. Y.; Lee, Y. S.; Kim, S. J.; Choy, J.
37 H.; Hwang, S. J. Mixed Valence Zn-Co-Layered Double Hydroxides and their Exfoliated
38 Nanosheets with Electrode Functionality. *J. Mater. Chem.* **2011**, *21*, 4286–4292.
39
40 (46) Huang, Z.; Wang, S.; Wang, J.; Yu, Y.; Wen, J., Li, R. Exfoliation-Restacking Synthesis of
41 CoAl-Layered Double Hydroxide Nanosheets/Reduced Graphene Oxide Composite for
42 High Performance Supercapacitors. *Electrochim. Acta* **2015**, *152*, 117–125.
43
44
45
46
47
48
49
50
51
52
53
54
55
56
57
58
59
60

- 1
2
3 (47) Wei, Y.; Cheng, G.; Xiong, J.; Xu, F.; Chen, R. Positive Ni(HCO₃)₂ as a Novel Cocatalyst
4 for Boosting the Photocatalytic Hydrogen Evolution Capability of Mesoporous TiO₂
5 Nanocrystals. *ACS Sustainable Chem. Eng.* **2017**, *5*, 5027–5038.
6
7
8 (48) Baliarsingh, N.; Mohapatra, L.; Parida, K. Design and Development of a Visible Light
9 Harvesting Ni-Zn/Cr-CO₃²⁻ LDH System for Hydrogen Evolution. *J. Mater. Chem. A*
10 **2013**, *1*, 4236–4243.
11
12
13 (49) Klopogge, J. T.; Frost, R. L. in *Layered Double Hydroxides: Present and Future*. ed.
14 Rives, V.Nova, New York, **2001**, p. 164.
15
16
17 (50) Rudolf, C.; Dragoi, B.; Ungureanu, A.; Chiriac, A.; Royer, S.; Nastro, A.; Dumitriu, E.
18 NiAl and CoAl Materials Derived from Takovite-Like LDHs and Related Structures as
19 Efficient Chemoselective Hydrogenation Catalysts. *Catal. Sci. Technol.* **2014**, *4*, 179–189.
20
21
22 (51) Qiu, Y.; Lin, B.; Jia, F.; Chen, Y.; Gao, B.; Liu, P. CdS-Pillared CoAl-Layered Double
23 Hydroxide Nanosheets with Superior Photocatalytic Activity. *Mater. Res. Bull.* **2015**, *72*,
24 235–240.
25
26
27 (52) Su, L. H.; Zhang, X. G. Effect of Carbon Entrapped in Co-Al Double Oxides on Structural
28 Restacking and Electrochemical Performances. *J. Power Sources* **2007**, *172*, 999–1006.
29
30
31 (53) Wang, Y.; Yang, W. S.; Zhang, S. C.; Evans, X.; Duan, D. G. Synthesis and
32 Electrochemical Characterization of Co-Al Layered Double Hydroxides. *J. Electrochem.*
33 *Soc.* **2005**, *152*, A2130–A2137.
34
35
36 (54) Tonda, S.; Kumar, S.; Gawli, Y.; Bhardwaj, M.; Ogale, S. B. g-C₃N₄ (2D)/CdS (1D)/rGO
37 (2D) Dual-Interface Nano-Composite for Excellent and Stable Visible Light Photocatalytic
38 Hydrogen Generation. *Int. J. Hydrogen Energy* **2017**, *42*, 5971–5984.
39
40
41 (55) Shao, M.; Ning, F.; Zhao, J.; Wei, M.; Evans, D. G.; Duan, X. Preparation of
42 Fe₃O₄@SiO₂@Layered Double Hydroxide Core-Shell Microspheres for Magnetic
43 Separation of Proteins. *J. Am. Chem. Soc.* **2012**, *134*, 1071–1077.
44
45
46 (56) Huang, X. H.; Li, G. H.; Cao, B. Q.; Wang, M.; Hao, C. Y. Morphology Evolution and CL
47 Property of Ni-Doped Zinc Oxide Nanostructures with Room-Temperature
48 Ferromagnetism. *J. Phys. Chem. C* **2009**, *113*, 4381–4385.
49
50
51 (57) Lu, X.; Ma, J.; Jiang, H.; Liu, C.; Lau, K. M. Low Trap States in In-Situ SiN_x/AlN/GaN
52 Metal-Insulator-Semiconductor Structures Grown by Metal-Organic Chemical Vapor
53 Deposition. *Appl. Phys. Lett.* **2014**, *105*, 102911.
54
55
56
57
58
59
60

- 1
2
3 (58) Dou, Y.; Zhang, S.; Pan, T.; Xu, S.; Zhou, A., Pu, M.; Yan, H.; Han, J.; Wei, M.; Evans, D.
4 G.; Duan, X. TiO₂@Layered Double Hydroxide Core–Shell Nanospheres with Largely
5 Enhanced Photocatalytic Activity Toward O₂ Generation. *Adv. Funct. Mater.* **2015**, *25*,
6 2243–2249.
7
8
9
10 (59) Bai, Y.; Chen, T.; Wang, P.; Wang, L.; Ye, L.; Shi, X.; Bai, W. Size-Dependent Role of
11 Gold in g-C₃N₄/BiOBr/Au System for Photocatalytic CO₂ Reduction and Dye Degradation.
12 *Sol. Energ. Mat. Sol. Cells* **2016**, *157*,406–414.
13
14
15 (60) Wang, J. C.; Yao, H. C.; Fan, Z. Y.; Zhang, L.; Wang, J. S.; Zang, S. Q.; Li, Z. J. Indirect
16 Z-Scheme BiOI/g-C₃N₄ Photocatalysts with Enhanced Photoreduction CO₂ Activity under
17 Visible Light Irradiation. *ACS Appl. Mater. Interfaces* **2016**, *8*, 3765–3775.
18
19
20 (61) Wang, Y.; Bai, X.; Qin, H.; Wang, F.; Li, Y.; Li, X.; Kang, S.; Zuo, Y.; Cui, L. Facile One-
21 Step Synthesis of Hybrid Graphitic Carbon Nitride and Carbon Composites as High-
22 Performance Catalysts for CO₂ Photocatalytic Conversion. *ACS Appl. Mater. Interfaces*
23 **2016**, *8*, 17212–17219.
24
25
26 (62) Li, M.; Zhang, L.; Fan, X.; Zhou, Y.; Wu, M.; Shi, J. Highly Selective CO₂ Photoreduction
27 to CO over g-C₃N₄/Bi₂WO₆ Composites under Visible Light. *J. Mater. Chem. A* **2015**, *3*,
28 5189–5196.
29
30
31 (63) Liu, S.; Weng, B.; Tang, Z. R.; Xu, Y. J. Constructing One-Dimensional Silver Nanowire
32 Doped Reduced Graphene Oxide Integrated with CdS Nanowire Network Hybrid
33 Structures toward Artificial Photosynthesis. *Nanoscale* **2015**, *7*, 861–866.
34
35
36 (64) Zhang, Q.; Li, Y.; Ackerman, E. A.; Josifovska, M. G.; Li, H. Visible Light Responsive
37 Iodine-Doped TiO₂ for Photocatalytic Reduction of CO₂ to Fuels. *Appl. Catal. A* **2011**,
38 *400*, 195–202.
39
40
41 (65) Wang, C.; Thompson, R. L.; Ohodnicki, P.; Baltrus, J.; Matranga, C. Size-Dependent
42 Photocatalytic Reduction of CO₂ with PbS Quantum Dot Sensitized TiO₂ Heterostructured
43 Photocatalysts. *J. Mater. Chem.* **2011**, *21*, 13452–13457.
44
45
46 (66) Zhou, H.; Guo, J.; Li, P.; Fan, T.; Zhang, D.; Ye, J. Leaf-Architected 3D Hierarchical
47 Artificial Photosynthetic System of Perovskite Titanates towards CO₂ Photoreduction into
48 Hydrocarbon Fuels. *Sci. Rep.* **2013**, *3*, 1667.
49
50
51
52
53
54
55
56
57
58
59
60

- 1
2
3 (67) Kuehnel, M. F.; Orchard, K. L.; Dalle, K. E.; Reisner, E. Selective Photocatalytic CO₂
4 Reduction in Water through Anchoring of a Molecular Ni Catalyst on CdS Nanocrystals. *J.*
5 *Am. Chem. Soc.* **2017**, *139*, 7217–7223.
6
7
8 (68) An, X.; Li, K.; Tang, J. Cu₂O/Reduced Graphene Oxide Composites for the Photocatalytic
9 Conversion of CO₂. *ChemSusChem* **2014**, *7*, 1086–1093.
10
11 (69) Ye, L.; Jin, X.; Liu, C.; Ding, C.; Xie, H.; Chu, K. H.; Wong, P. K. Thickness-Ultrathin
12 and Bismuth-Rich Strategies for BiOBr to Enhance Photoreduction of CO₂ into Solar
13 Fuels, *Appl. Catal. B Environ.* **2016**, *187*, 281–290.
14
15 (70) Ye, L.; Wang, H.; Jin, X.; Su, Y.; Wang, D.; Xie, H.; Liu, X.; Liu, X. Synthesis of Olive-
16 Green Few-Layered BiOI for Efficient Photoreduction of CO₂ into Solar Fuels under
17 Visible/Near-Infrared Light. *Sol. Energy Mater Sol. Cells*, **2016**, *144*, 732–739.
18
19 (71) Tian, L.; Zhao, Y.; He, S.; Wei, M.; Duan, X. Immobilized Cu–Cr Layered Double
20 Hydroxide Films with Visible-Light Responsive Photocatalysis for Organic Pollutants.
21 *Chem. Eng. J.* **2012**, *184*, 261–267.
22
23
24
25
26
27
28
29
30
31
32
33
34
35
36
37
38
39
40
41
42
43
44
45
46
47
48
49
50
51
52
53
54
55
56
57
58
59
60

Figure Captions

Scheme 1. Schematic illustration of the synthesis process of g-C₃N₄/NiAl-LDH hybrid heterojunctions.

Figure 1. XRD patterns of the synthesized g-C₃N₄, NiAl-LDH, and g-C₃N₄/NiAl-LDH heterojunctions.

Figure 2. UV–vis DRS of g-C₃N₄, NiAl-LDH, and g-C₃N₄/NiAl-LDH heterojunction samples.

Figure 3. FT-IR spectra of g-C₃N₄, NiAl-LDH, and g-C₃N₄/NiAl-LDH heterojunction samples.

Figure 4. TEM images of (a) NiAl-LDH, (b) g-C₃N₄, (c, d and e) CNLDH-10, and (f) HRTEM image of the CNLDH-10 heterojunction.

Figure 5. XPS profiles of (a) N 1s, (b) C 1s, (c) Ni 2p, and (d) Al 2p of g-C₃N₄, NiAl-LDH and CNLDH-10 samples.

Figure 6. Time-dependent (a) CO, (b) H₂, and (c) O₂ amounts generated over all the synthesized photocatalysts (Conditions: 50 mg catalyst and 300 W Xenon lamp with a UV cut-off filter ($\lambda \geq 420$ nm)). (d) An action spectrum of AQY on account of CO production by CNLDH-10 photocatalyst (blue plot), along with DRS of CNLDH-10 (green curve).

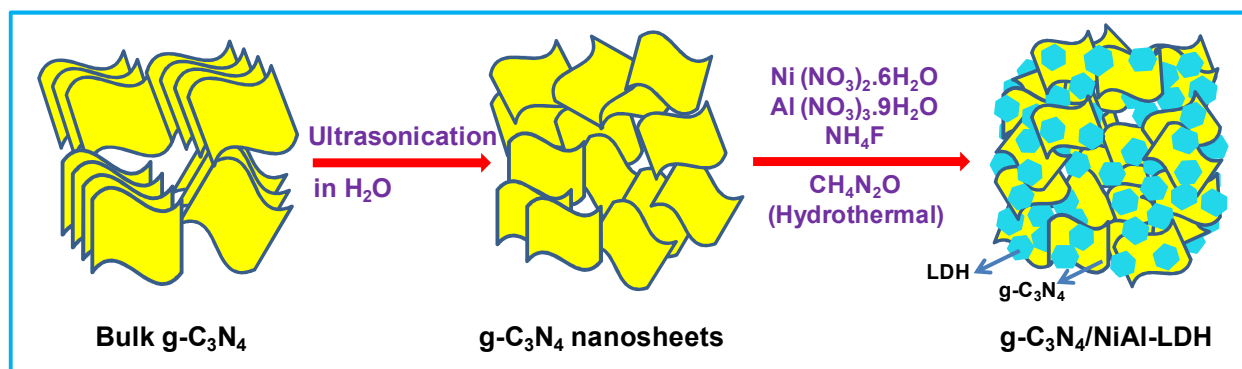
Figure 7. Reusability studies of CO evolution over CNLDH-10 heterojunction.

Figure 8. (a) PL spectra and (b) transient photocurrent responses of g-C₃N₄, NiAl-LDH, and g-C₃N₄/NiAl-LDH heterojunction photocatalysts.

Figure 9. Valence band XP spectra of g-C₃N₄ and NiAl-LDH samples.

Figure 10. Schematic illustration of the proposed mechanism for CO₂ photoreduction in the g-C₃N₄/NiAl-LDH heterojunctions.

Figures



Scheme 1. Schematic illustration of the synthesis process of g-C₃N₄/NiAl-LDH hybrid heterojunctions.

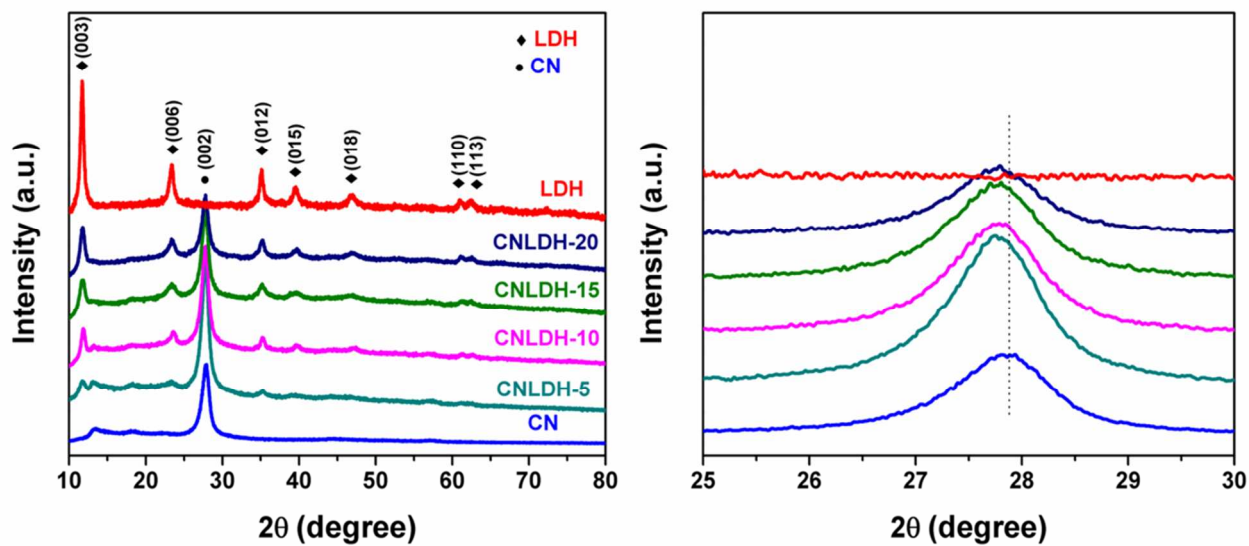


Figure 1. XRD patterns of the synthesized $g\text{-C}_3\text{N}_4$, NiAl-LDH, and $g\text{-C}_3\text{N}_4/\text{NiAl-LDH}$ heterojunctions.

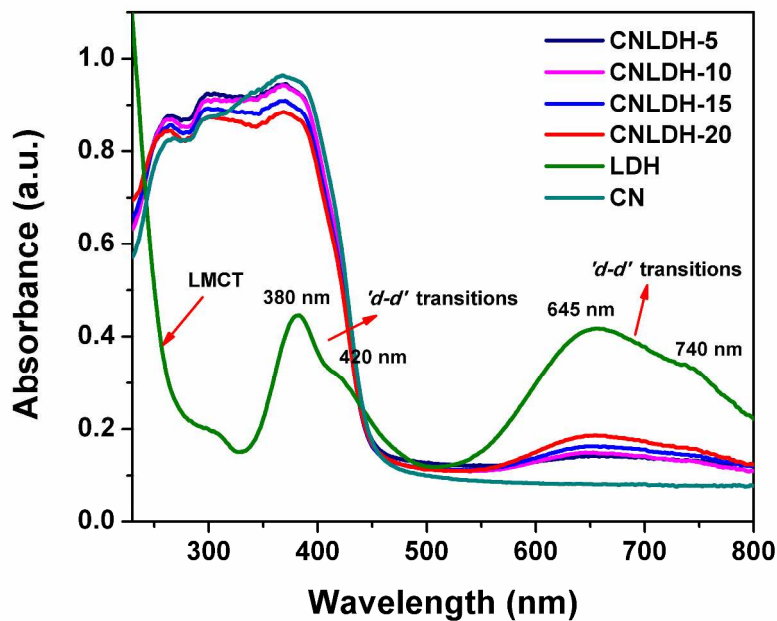


Figure 2. UV-vis DRS of g-C₃N₄, NiAl-LDH, and g-C₃N₄/NiAl-LDH heterojunction samples.

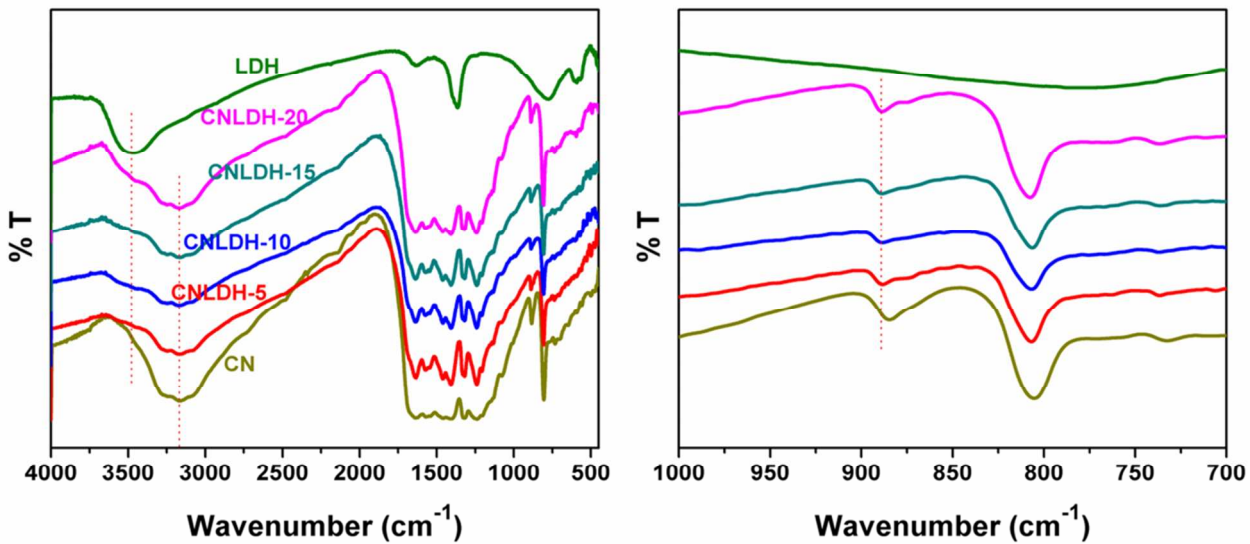


Figure 3. FT-IR spectra of g-C₃N₄, NiAl-LDH, and g-C₃N₄/NiAl-LDH heterojunction samples.

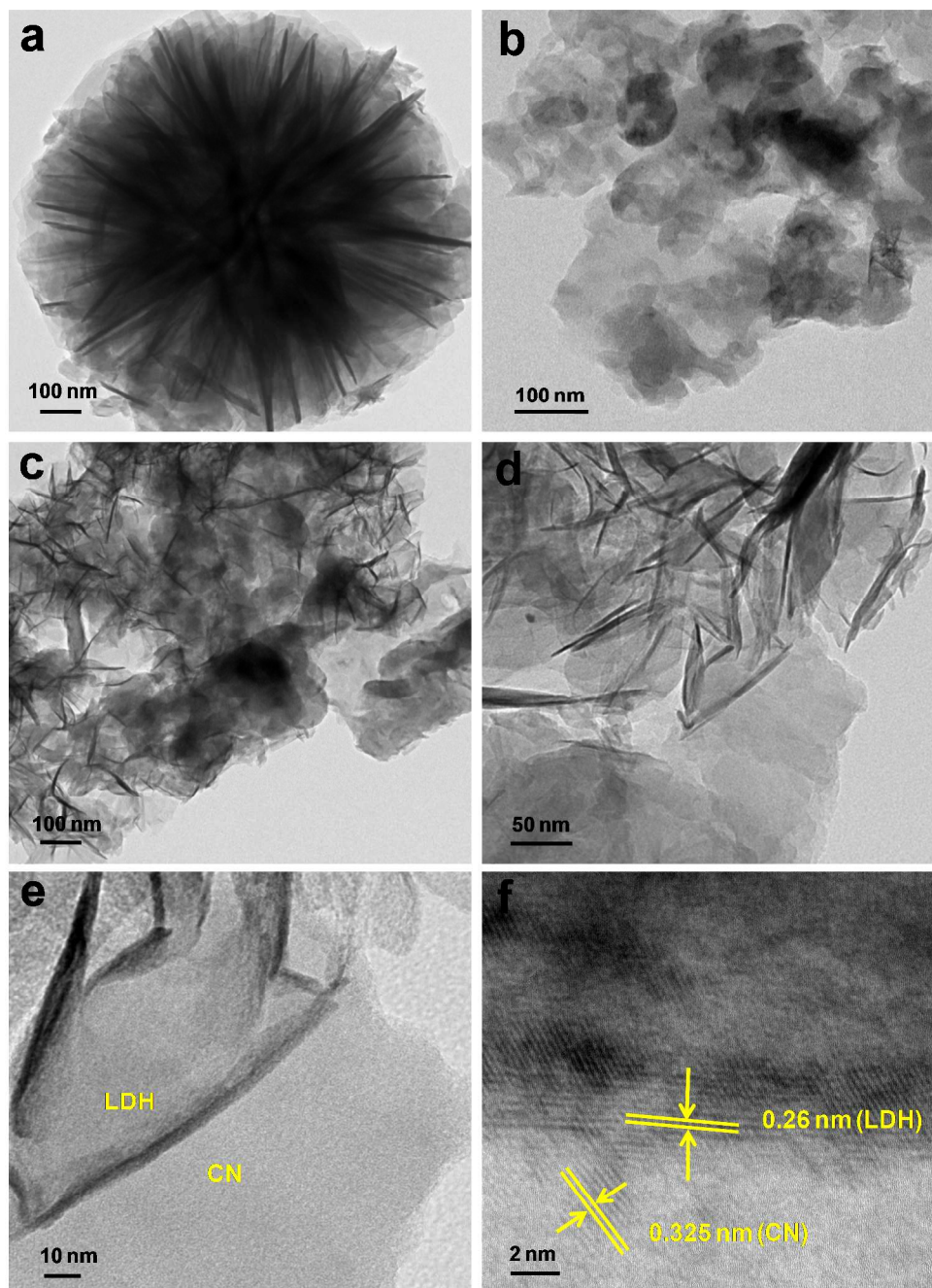


Figure 4. TEM images of (a) NiAl-LDH, (b) g-C₃N₄, (c, d and e) CNLDH-10, and (f) HRTEM image of the CNLDH-10 heterojunction.

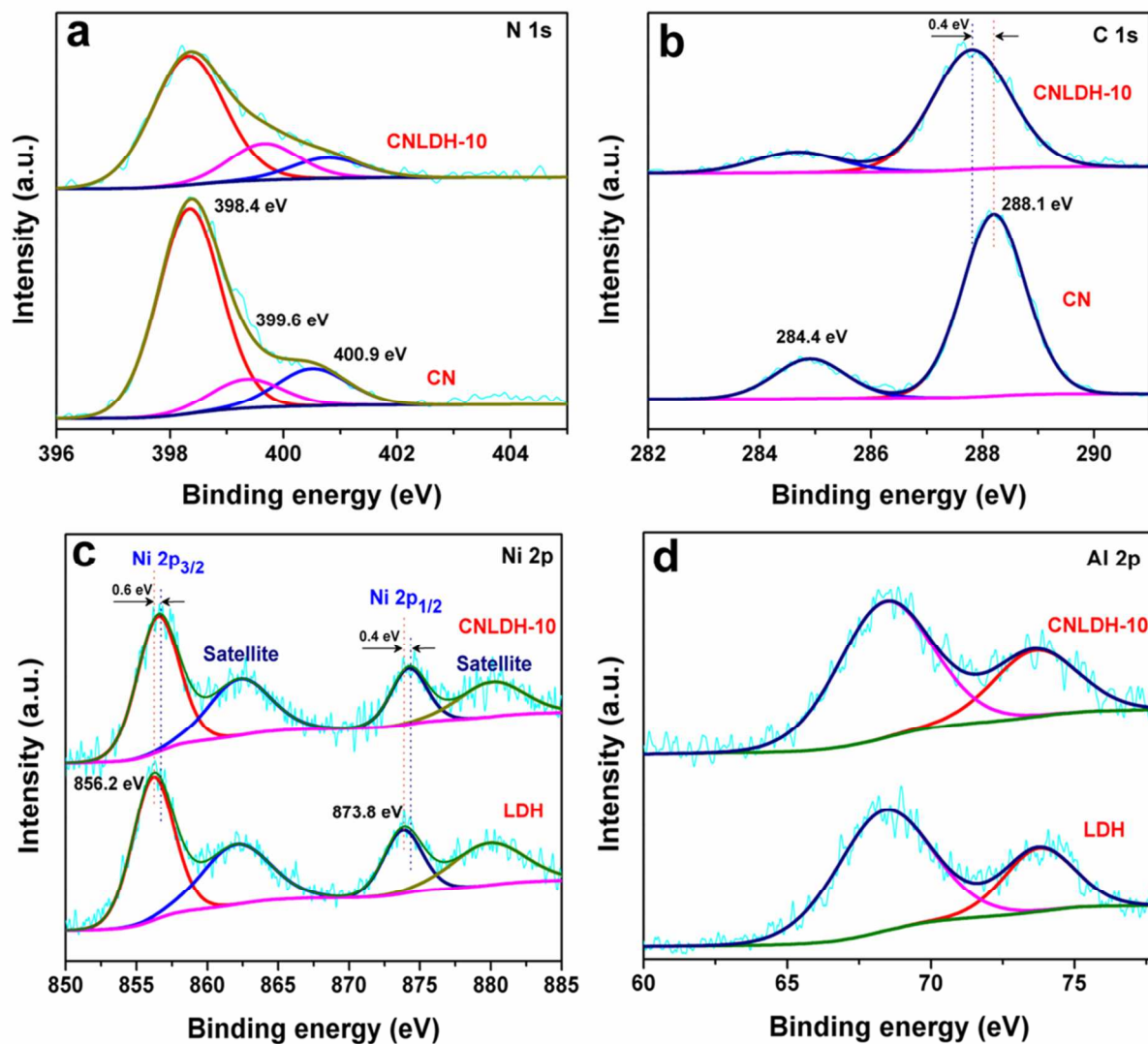


Figure 5. XPS profiles of (a) N 1s, (b) C 1s, (c) Ni 2p, and (d) Al 2p of g-C₃N₄, NiAl-LDH and CNLDH-10 samples.

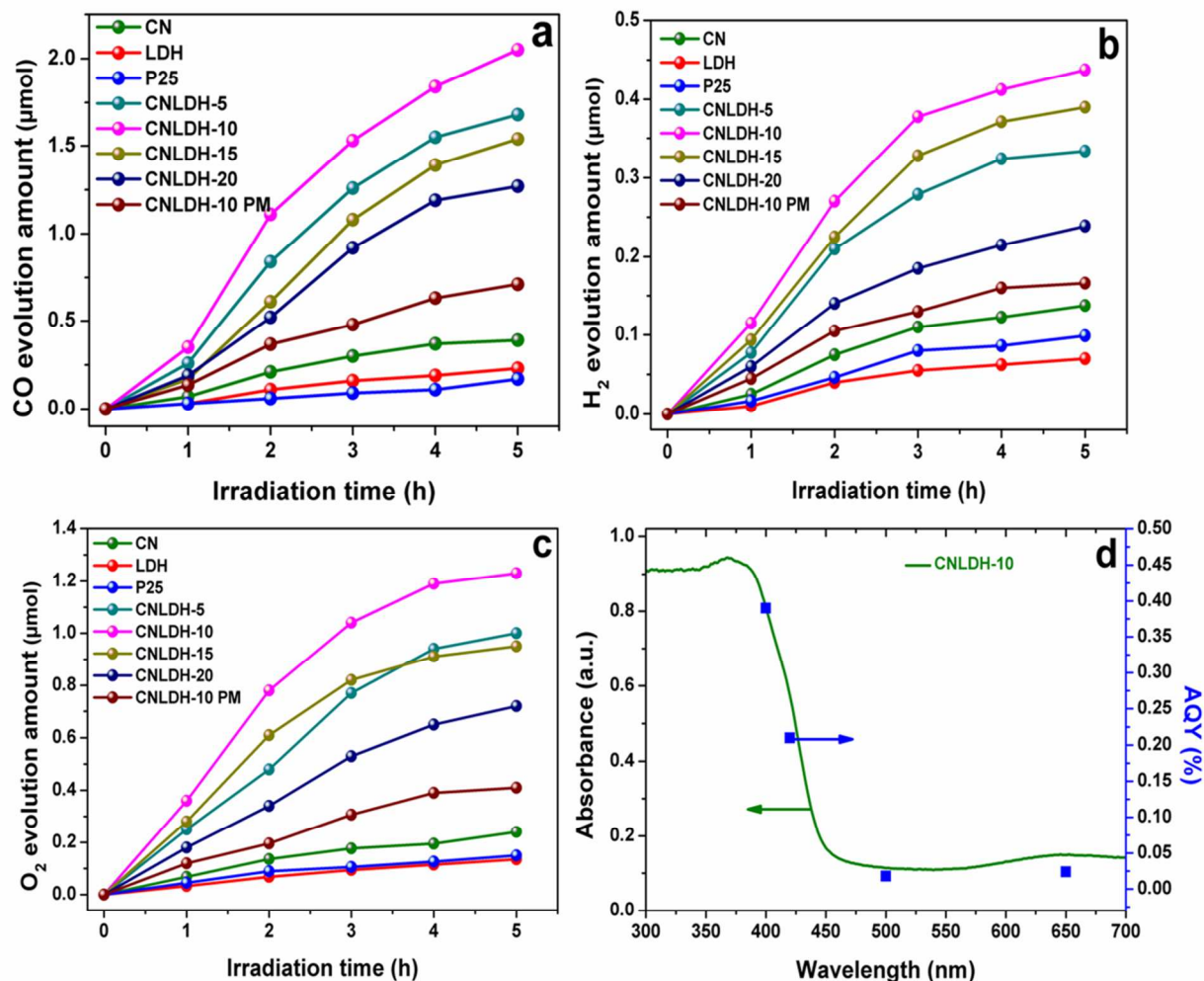


Figure 6. Time-dependent (a) CO, (b) H₂, and (c) O₂ amounts generated over all the synthesized photocatalysts (Conditions: 50 mg catalyst and 300 W Xenon lamp with a UV cut-off filter ($\lambda \geq 420$ nm)). (d) An action spectrum of AQY on account of CO production by CNLDH-10 photocatalyst (blue plot), along with DRS of CNLDH-10 (green curve).

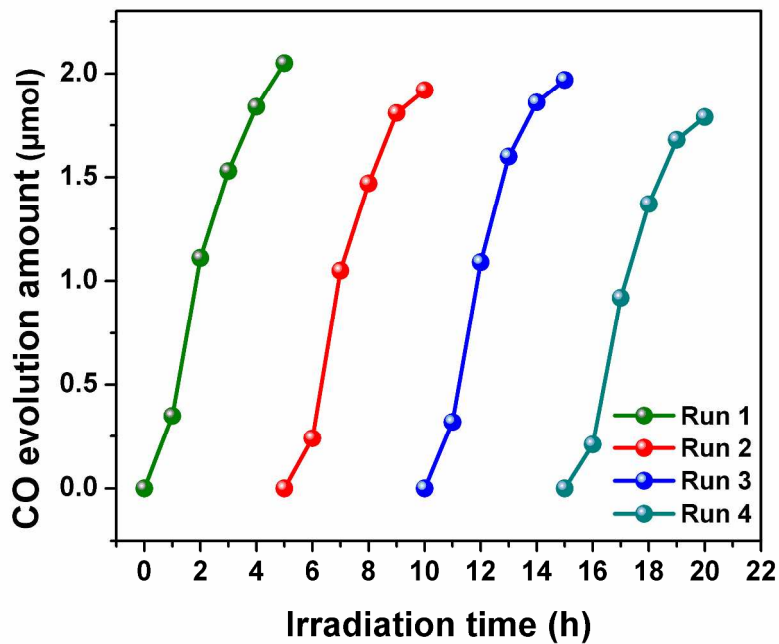


Figure 7. Reusability studies of CO evolution over CNLDH-10 heterojunction.

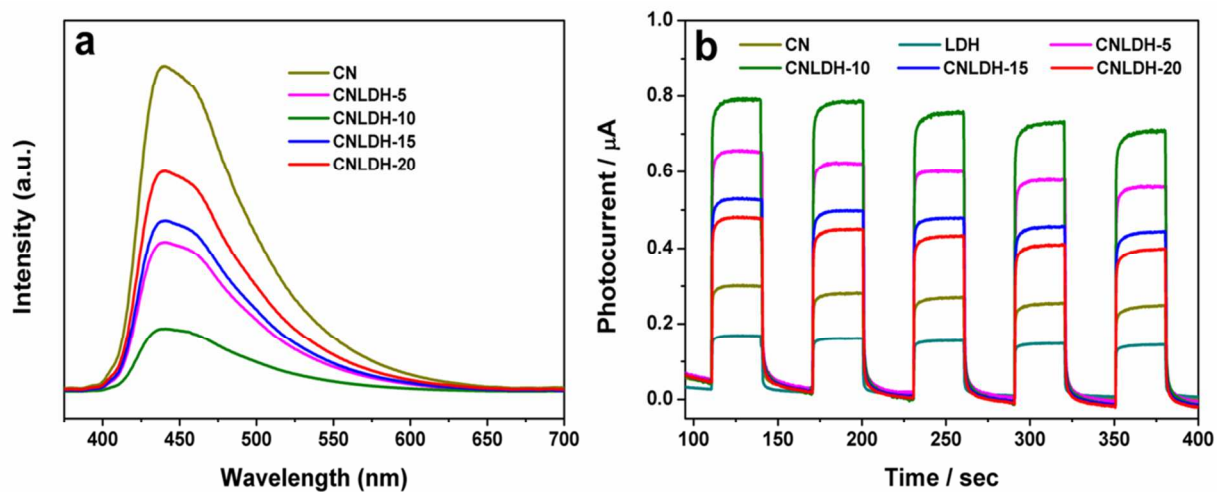


Figure 8. (a) PL spectra and (b) transient photocurrent responses of g-C₃N₄, NiAl-LDH, and g-C₃N₄/NiAl-LDH heterojunction photocatalysts.

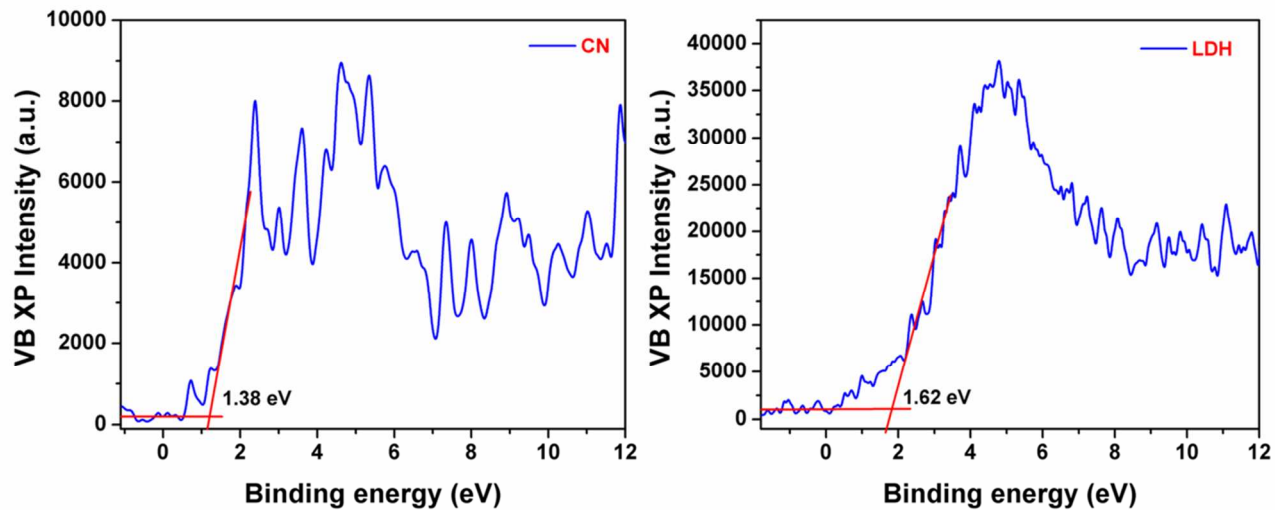


Figure 9. Valence band XP spectra of g-C₃N₄ and NiAl-LDH samples.

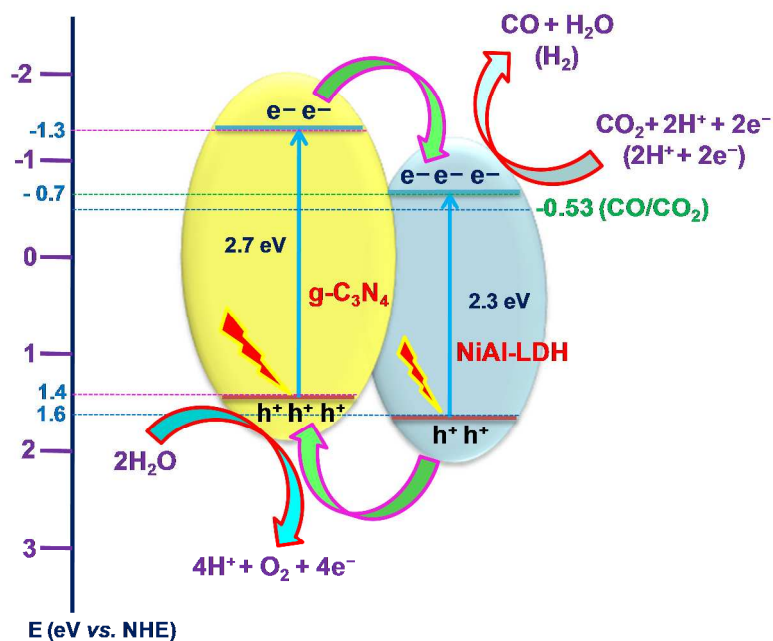
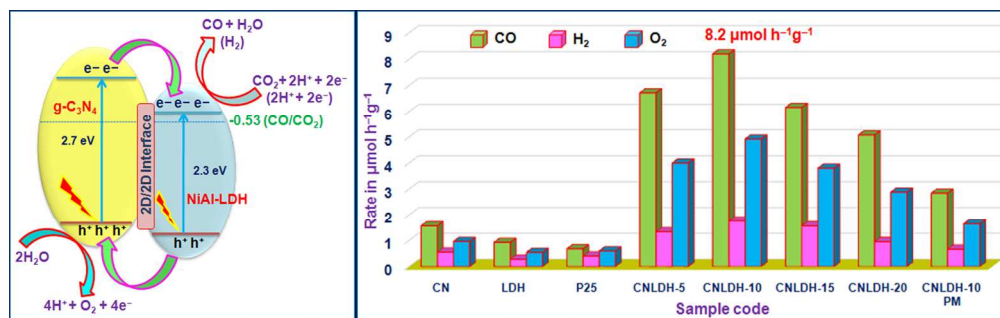


Figure 10. Schematic illustration of the proposed mechanism for CO_2 photoreduction in the $g\text{-C}_3\text{N}_4/\text{NiAl-LDH}$ heterojunctions.



322x100mm (300 x 300 DPI)